Check for updates

Received: 5 January 2022 | Revised: 23 March 2022 | Accepted: 8 June 2022

DOI: 10.1002/jbm.b.35124

RESEARCH ARTICLE

Society For Biomaterials | WILEY

Laser-induced heating of polydimethylsiloxane-magnetite nanocomposites for hyperthermic inhibition of triple-negative breast cancer cell proliferation

Chinyerem E. Onyekanne[1] | Ali A. Salifu[2,3] | John D. Obayemi[2,3] | Chukwuemeka J. Ani[4] | Habibeh Ashouri Choshali[5] | Chukwudalu C. Nwazojie[1] | Killian C. Onwudiwe[1] | Josephine C. Oparah[1] | Theresa C. Ezenwafor[1] | Chukwudi C. Ezeala[1] | Olushola S. Odusanya[1,6] | Nima Rahbar[5] | Winston O. Soboyejo[1,2,3]

[1]Department of Materials Science and Engineering, Biomaterials Lab, African University of Science and Technology, Abuja, Federal Capital Territory, Nigeria

[2]Department of Mechanical Engineering, Worcester Polytechnic Institute, Worcester, Massachusetts, USA

[3]Department of Biomedical Engineering, Worcester Polytechnic Institute, Worcester, Massachusetts, USA

[4]Department of Physics, Nile University of Nigeria, Abuja, Federal Capital Territory, Nigeria

[5]Department of Civil and Environmental Engineering, Worcester Polytechnic Institute, Worcester, Massachusetts, USA

[6]Biotechnology and Genetic Engineering Advanced Laboratory, Sheda Science and Technology Complex, Abuja, Federal Capital Territory, Nigeria

Correspondence
Winston O. Soboyejo, Worcester Polytechnic Institute, 100 Institute Road, Worcester, MA 01609, USA.
Email: wsoboyejo@wpi.edu

Funding information
Pan African Materials Institute, Grant/Award Number: P126974; Worcester Polytechnic Institute; World Bank African Centers of Excellence

Abstract

This paper presents the results of an experimental and computational study of the effects of laser-induced heating provided by magnetite nanocomposite structures that are being developed for the localized hyperthermic treatment of triple-negative breast cancer. Magnetite nanoparticle-reinforced polydimethylsiloxane (PDMS) nanocomposites were fabricated with weight percentages of 1%, 5%, and 10% magnetite nanoparticles. The nanocomposites were exposed to incident Near Infrared (NIR) laser beams with well-controlled powers. The laser-induced heating is explored in: (i) heating liquid media (deionized water and cell growth media [Leibovitz L15+]) to characterize the photothermal properties of the nanocomposites, (ii) in vitro experiments that explore the effects of localized heating on triple-negative breast cancer cells, and (iii) experiments in which the laser beams penetrate through chicken tissue to heat up nanocomposite samples embedded at different depths beneath the chicken skin. The resulting plasmonic laser-induced heating is explained using composite theories and heat transport models. The results show that the laser/nanocomposite interactions decrease the viability of triple-negative breast cancer cells (MDA-MB-231) at temperatures in the hyperthermia domain between 41 and 44°C. Laser irradiation did not cause any observed physical damage to the chicken tissue. The potential in vivo performance of the PDMS nanocomposites was also investigated using computational finite element models of the effects of laser/magnetite nanocomposite interactions on the temperatures and thermal doses experienced by tissues that surround the nanocomposite devices. The implications of the results are then discussed for the development of implantable nanocomposite devices for localized treatment of triple-negative breast cancer tissue via hyperthermia.

KEYWORDS
hyperthermia, laser-induced heating, PDMS-magnetite nanocomposites, triple-negative breast cancer

 © 2022 Wiley Periodicals LLC.

15524981, 2022, 12, Downloaded from https://onlinelibrary.wiley.com/doi/10.1002/jbm.b.35124 by Egyptian National Sci. Network (Enstinet), Wiley Online Library on [08/11/2022]. See the Terms and Conditions (https://onlinelibrary.wiley.com/terms-and-conditions) on Wiley Online Library for rules of use; OA articles are governed by the applicable Creative Commons License

1 | INTRODUCTION

The increasing incidence of cancer[1–3] has stimulated the development of alternative therapies that reduce the side effects associated with cancer treatment.[4–7] Breast cancer is one of the most common diseases in women across the world.[8] In the case of women in developing countries, breast cancer is the second leading cause of cancer mortality.[8,9] There is, therefore, a need for improved methods for the detection and treatment of breast cancer.

Conventional treatments that have been explored include surgery, chemotherapy, radiotherapy, hormonal therapy, and so forth.[10–12] However, these techniques are associated with severe side effects.[12–14] Furthermore, although the surgical removal of the solid tumors may be effective for the removal of well-defined and accessible primary tumors located within non-vital tissues, surgical resection is less suitable for the treatment of small and less well-defined tumors and metastases, or tumors embedded within organs.[15] Residual tumor tissues are also left behind in most cases after cancer surgery.

Since these residual tumors may evolve ultimately into metastatic tumors,[16] there is a need for alternative approaches to the treatment of residual tumor tissue that is left behind after surgical removal of breast tumor tissue. This has stimulated several research groups to develop implantable devices for localized cancer drug release[17–19] or the hyperthermic heating of breast cancer cells/tissues.[13,20–24] The latter include heating by resistive Joule heating,[23] inductive heating,[24–27] and plasmonic heating by laser beam interactions with gold,[28] silver,[29,30] and copper nanoparticles.[31]

Nanomaterial-mediated hyperthermia has been studied with different energy sources such as radio-frequency and microwave, focused ultrasound, infrared lasers, and visible light lasers[29] (visible light lasers are associated with surface plasmon resonance (SPR) effects that make them better candidates for hyperthermic treatment of deep-seated tumors[29]). In most cases, many of the prior studies have focused on laser interactions with Au, Ag, and Cu nanoparticles.[29–32] However, more recently, magnetite nanoparticles (MNPs) have been shown to be promising agents for photothermal heating under near-infrared irradiation (NIR) conditions.[29–35]

PDMS is inert, highly biocompatible and structurally stable in the tissue environment.[36] It is also a thermally stable biomaterial that exhibits little viscosity changes upon changes in temperature. These are in addition to its corrosion resistance and flexible properties.[36,37] Hence, this work examines the effects of laser-induced heating of magnetite-reinforced PDMS nanocomposites for hyperthermia (41–44°C).[26,38–41] The PDMS nanocomposites (NCs) were molded and the effects of MNP content on the photothermal properties of the NCs under in vitro conditions were then investigated. First, the laser-induced heating effects of the various nanocomposites are explored in deionized water and cell culture growth media. The effects of laser-induced nanocomposites heating on MDA-MB-231 triple-negative breast cancer cell line are then elucidated in in vitro studies of cell viability (alamar blue assay and live/dead cell double fluorescence staining) and the quantification of heat shock protein release from stressed cells. The ability of the laser beam to penetrate through chicken tissue to heat up PDMS nanocomposites samples (placed at different depths beneath the chicken skin) is also explored.

Furthermore, in an effort to investigate the in vivo performances of the nanocomposites and its thermal profile, a three-dimensional finite element model (3D FEM) was also developed. The predictions from the FEM model are then validated before discussing the implications of the results for the use of MNP reinforced PDMS nanocomposites in the localized treatment of triple-negative breast cancer.

2 | MATERIALS AND METHODS

2.1 | Materials

PDMS Sylgard 184 silicone elastomer kit was procured from Dow Corning Corporation (Auburn, MI), while magnetite (iron oxide; Fe_3O_4) nanopowder (high purity, 99.5%, 15–20 nm size range) was purchased from US Research Nanomaterials (Houston, TX). The combination of the PDMS and MNP powder were mixed for the fabrication of the polymer nanocomposite samples. All of the chemicals were used in the as-received condition. Human triple-negative breast cancer cell line (MDA-MB-231) was obtained from the American Type Culture Collection (Manassas, VA). Leibovitz L15 medium, fetal bovine serum (FBS), penicillin/streptomycin antibiotic, 0.25% trypsin–EDTA, and DMEM/Ham's F12 medium (1:1) were procured from Thermo Fisher Scientific (Waltham, MA). All other cell culture reagents were procured from Thermo Fisher Scientific, unless otherwise stated.

2.2 | Fabrication and physicochemical characterization of PDMS-magnetite nanocomposites

The MNPs were mixed with PDMS to obtain nanocomposites containing 1, 5, and 10 wt% of MNPs. Initially, the base kit of the PDMS elastomer was mixed with the curing agent at a weight ratio of 10:1. The mixture was then stirred to obtain a uniform mixture after which the powdered MNPs were added. The resulting mixtures were stirred and poured into molds (100 mm × 15 mm Petri dishes) before degassing at room temperature (approximately 25°C) to remove trapped air bubbles. This was done for 30 min at a pressure of approximately 25 mmHg in a vacuum oven. Finally, the cast PDMS-MNP mixtures were cured for 4 h at 60°C in the vacuum oven to produce the PDMS nanocomposites.

The nanocomposites were carefully removed from the molds and characterized using Fourier transform infrared (FTIR) spectroscopy and scanning electron microscopy (SEM). The FTIR spectra of the samples were obtained from an FTIR spectrometer (IRSpirit, Shimadzu, Kyoto, Japan) from an average of 128 scans at a resolution of 2 cm^{-1} over the wavenumber range from 400 to 4000 cm^{-1}. The surface morphology of the PDMS nanocomposites was observed under a

15524981, 2022, 12, Downloaded from https://onlinelibrary.wiley.com/doi/10.1002/jbm.b.35124 by Egyptian National Sci. Network (Enstinet), Wiley Online Library on [08/11/2022]. See the Terms and Conditions (https://onlinelibrary.wiley.com/terms-and-conditions) on Wiley Online Library for rules of use; OA articles are governed by the applicable Creative Commons License

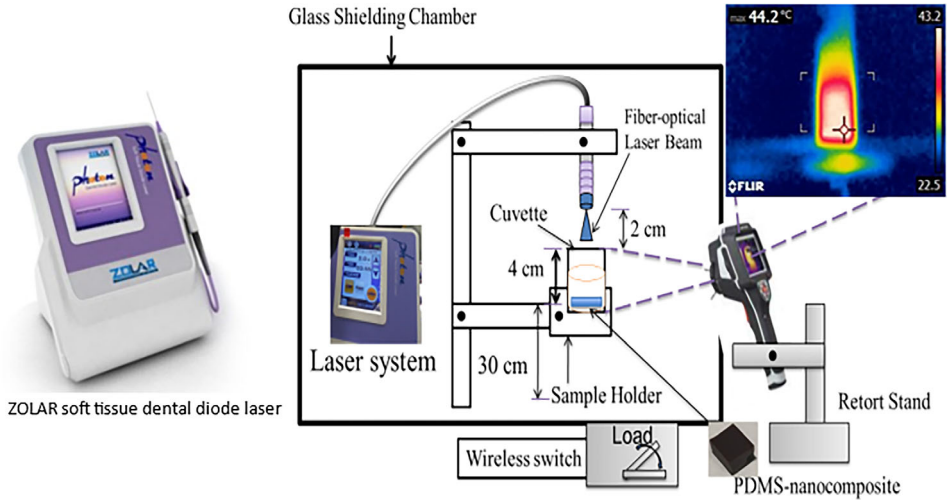


FIGURE 1 A schematic of the setup for the laser heating of the PDMS-MNP nanocomposites

Phenom G1 Scanning Electron Microscope, equipped with a backscatter electron detector, at an accelerating voltage of 5 kV.

2.3 | Laser-induced heating of the PDMS-magnetite nanocomposites

The PDMS nanocomposites were cut into 5 mm × 5 mm × 5 mm cubes and the laser-induced heating experiments were carried out using the set-up summarized in Figure 1. This consisted of a Photon 3W Dental Diode Laser (Zolar Technology and Manufacturing, Mississauga, ON, Canada) emitting a near infrared laser light beam ($\lambda = 810$ nm). The laser beam was transmitted through a fiber optic cable to the tip of a cylindrical probe before propagating into the samples placed in plastic cuvettes (4 cm high × 1 cm wide). The distance between the tip of the probe and the cuvette was set at 2 cm to achieve a laser spot size of 1 cm on the samples. In initial experiments to characterize the photothermal properties of the nanocomposites, the samples (5 mm × 5 mm × 5 mm) were immersed in either 1 ml of deionized water or 1 ml of cell growth medium (Leibovitz L15+ medium) in the cuvette and exposed to the 810 nm laser beam for 20 min. The laser beam propagated through the nanocomposites and interacted with the MNPs to generate heat leading to a gradual temperature rise. The temperature distributions across the nanocomposite samples and the surrounding liquid media (deionized water and L15+ medium) were recorded every minute using an infrared (IR) thermal camera (FLIR E4 Thermal Imaging Camera, FLIR Systems, Wilsonville, OR). After 20 min of heating, the laser beam was switched off and the cooling temperature values were recorded at 30 s intervals. The maximum temperature values were used to plot the heating and cooling temperature profiles of the samples. We experimented with laser powers of 0.6, 1.0, 1.5, and 2.0 W to optimize the laser powers capable of generating temperatures in the hyperthermia domain (41–44°C). Plain PDMS (without MNPs) was treated under the same conditions above as controls, and all samples were subjected to one laser-induced heating cycle.

2.4 | Biological characterization

2.4.1 | Cell culture

The human triple-negative breast cancer (MDA-MB-231) cells were grown in Leibovitz L15 medium supplemented with 10% FBS, 100 IU/ml penicillin, and 100 μg/ml streptomycin (referred to as L15+ medium) in T75 flasks. The flasks were then incubated in a humidified incubator set at 37°C (without CO_2). Upon reaching 80%–90% confluence, the cells were detached using the 0.25% trypsin–EDTA solution and sub cultured in fresh T75 flasks at a passage ratio of 1:4. MDA-MB-231 cells between passages 6 and 7 were harvested at 80%–90% confluence and used for the cell viability, live/dead cell double staining, and heat shock protein release studies described below.

2.4.2 | Cell viability studies

To assess the effect of the laser-induced heating of the PDMS nanocomposites on the viabilities of the MDA-MB-231 cells, the nanocomposites (and plain PDMS) were immersed in 1 ml of L15+ medium containing 100,000 cells in the cuvettes and heated with a 0.6 W laser beam for 30 min under aseptic conditions in a biosafety cabinet. Cells only without nanocomposites (i.e., 100,000 cells in 1 ml L15+ medium in the cuvette) were also exposed to the 0.6 W laser for 30 min as a control (herein referred to as "cells + heating"). The nanocomposite and plain PDMS samples were also immersed in the 1 ml cell suspension in L15+ medium for 30 min as controls (herein referred to as "soaked sample controls"). Prior to the experiments, the samples and the cuvettes were sterilized with 70% ethanol and rinsed 5× with phosphate-buffered saline.

The laser power of 0.6 W resulted in temperatures in the hyperthermia domain (41–44°C). After the laser heating, the nanocomposites were removed from the cuvettes and the cells (in the L15+ medium) were transferred into sterile ventilated tubes and

15524981, 2022, 12, Downloaded from https://onlinelibrary.wiley.com/doi/10.1002/jbm.b.35124 by Egyptian National Sci. Network (Enstinet), Wiley Online Library on [08/11/2022]. See the Terms and Conditions (https://onlinelibrary.wiley.com/terms-and-conditions) on Wiley Online Library for rules of use; OA articles are governed by the applicable Creative Commons License

incubated at 37°C (without CO_2) for 12 h. Untreated cells (i.e., 100,000 cells in 1 ml L15+ medium) were also transferred into ventilated tubes and incubated at 37°C (without CO_2) for 12 h to serve as the baseline (herein referred to as "cells only"). Subsequently, cell viability was assessed indirectly by measuring the metabolic activities of the cells using the alamar blue assay (Thermo Fisher Scientific, Waltham, MA), which relies on the conversion of the nonfluorescent resazurin into a highly fluorescent resorufin by metabolically active cells.

The tubes were centrifuged at 900 rpm for 5 min and the supernatants were transferred into separate tubes to be used for the heat shock protein release studies (described below). The cell pellets were then resuspended in 0.4 ml of L15+ medium containing 10% of the alamar blue reagent and incubated at 37°C (without CO_2) for 3 h. Afterward, 100 μl aliquots were transferred into a black 96-well plate (Thermo Fisher Scientific) and the fluorescence intensities of the samples were measured using a 1420 Victor 3 multi-label plate reader (Perkin Elmer, Waltham, MA) at 544/590 nm (excitation/emission). To isolate the effects of hyperthermia-induced cell growth inhibition from sample-induced inhibition, the readings from the "soaked sample controls" were subtracted from the corresponding readings from the heated samples to obtain corrected fluorescence intensities for each sample. The corrected fluorescence values were then used to calculate the percentage cell growth inhibition due to laser-induced hyperthermia using Equation (1).

$$\%\ \text{Growth Inhibition} = \left(1 - \frac{FI_{samples}}{FI_{cells}}\right) \times 100 \quad (1)$$

where, $FI_{samples}$ is the fluorescence intensity of the samples and FI_{cells} is the fluorescence intensity of the untreated cells.

2.4.3 | Live/dead cell staining

Live and dead cells were visualized after the laser-induced heating of the nanocomposites to assess the effects of hyperthermia on the cells. The cells were stained using a live/dead cell double staining kit (Sigma-Aldrich, St. Louis, MI) that consisted of nonfluorescent solutions of acetoxymethyl ester of calcein (Calcein-AM) and propidium iodide (PI) for the simultaneous fluorescent labeling of live (green) and dead (red) cells. Calcein-AM permeates live cell membranes and gets hydrolyzed into a green fluorescent calcein product whereas PI only passes through damaged dead cell membranes and interacts with the DNA double helix to generate red-fluorescent PI-DNA complexes. Following the same procedure as the cell viability studies, the cell pellets obtained were resuspended in 20 μl of an assay solution (comprising of calcein-AM, PI and PBS) that was prepared according to the manufacturer's instructions. The cell suspension was incubated at 37°C for 15 min, placed on a glass slide, and covered with a coverslip. Live and dead cells were then imaged using an Eclipse Ts2R fluorescence microscope (Nikon, Tokyo, Japan).

2.4.4 | Heat shock protein release

The amounts of the heat shock protein HSP70 released from the cells into the L15+ medium after exposure of the cells to the laser-induced hyperthermic temperatures were quantified using the Human HSP70 ELISA kit (Thermo Fisher Scientific, Waltham, MA) according to the manufacturer's instructions. This was carried out to investigate whether the MDA-MB-231 triple negative breast cancer cells were stressed by the laser-induced hyperthermia conditions, resulting in decreased cell viabilities.

Briefly, 50 μl of the supernatants obtained after centrifugation at 900 rpm for 5 min (see the procedure under cell viability studies) were first incubated with 50 μl of Sample Diluent in the ELISA microplate wells at room temperature (approximately 25°C) for 2 h on an orbital shaker. About 50 μl of L15+ medium was also incubated with 50 μl Sample Diluent in blank wells. This was followed by serial incubations (approximately25°C) with 100 μl Biotin-Conjugate Solution (1 h on orbital shaker), 100 μl Streptavidin-HRP Solution (30 min on orbital shaker), and 100 μl TMB Substrate Solution (30 min in the dark). The microplate wells were washed 5× with the Wash Buffer between the steps.

Finally, 100 μl Stop Solution was added to the wells and the absorbance of each well was measured at 450 nm using the 1420 Victor 3 multi-label plate reader. Readings from the blank wells were subtracted from the sample wells to obtain corrected absorbance values. The amounts of the HSP70 protein in the wells were then interpolated from a standard curve generated from HSP70 protein standards.

2.5 | Laser-induced heating of the PDMS nanocomposites in a chicken model

The ability of the NIR laser beam to penetrate tissue and heat nanocomposite samples buried in the tissue was investigated using a chicken model. Chicken was selected due to the closeness of the emissivity coefficients (ε) of chicken ($\varepsilon \approx 0.95$)[42,43] and human skin ($\varepsilon \approx 0.98$).[44] Chicken thighs were purchased from a local supermarket. The skin around the area of interest (away from the bones) was lifted up to expose the flesh underneath. Approx. 1 cm diameter incisions were made on the flesh, and the tissue was cut out to create grooves. The nanocomposite samples were then buried in the grooves at depths of 2 and 8 mm beneath the skin and covered with the cut-out tissue followed by the skin.

Subsequently, the effect of laser penetration through the tissue was studied by focusing the laser beam with different powers (0.6, 1.0, and 3.0 W) on the skin directly above the buried nanocomposite samples. The laser probe was clamped vertically 2 cm above the skin to create a spot size of 1 cm. The laser beam was applied for 20 min, and increases in the surface temperature emanating from the laser-induced heating of the nanocomposites buried in the tissue were monitored with the IR thermal camera.

15524981, 2022, 12, Downloaded from https://onlinelibrary.wiley.com/doi/10.1002/jbm.b.35124 by Egyptian National Sci. Network (Enstinet), Wiley Online Library on [08/11/2022]. See the Terms and Conditions (https://onlinelibrary.wiley.com/terms-and-conditions) on Wiley Online Library for rules of use; OA articles are governed by the applicable Creative Commons License

TABLE 1 Polydimethylsiloxane and magnetite nanoparticle parameters used for the simulations

Parameter	Value	Ref.
PDMS: Density, ρ	0.97 kg m^{-3}	[80]
PDMS: Heat capacity, C_p	1.46 kJ kg^{-1} K^{-1}	[80]
PDMS: Thermal conductivity, λ	0.15 W m^{-1} K^{-1}	[80]
PDMS: Absorption coefficient, μ_a	0.988 m^{-1}	[81]
MNP: Density, ρ	5180 kg m^{-3}	[82]
MNP: Heat capacity, C_p	0.671 kJ kg^{-1} K^{-1}	[82]
MNP: Thermal conductivity, λ	6.0 W m^{-1} K^{-1}	[82]

2.6 | Statistical analysis

Unless otherwise stated, the results are reported as mean ± standard deviation for three independent trials ($n = 3$). Differences in photothermal and biological properties between the PDMS-MNP nanocomposite groups were analyzed using one-way ANOVA with post hoc Bonferroni tests using IBM SPSS Statistics 25 package. The differences were considered significant at p-values less than .05.

3 | MODELING

The model system that was explored in this work consists of a laser source with a fiber optic delivery system (Figure 1). This was connected to an 810 nm near infrared laser light source with an intensity of 10^4 W m^{-2}.[45] The light was transmitted through the fiber optic system to the active tip surface of the cylindrical probe before propagating through the polymer nanocomposite/tissue model. As the light propagates through the PDMS nanocomposite, it is absorbed by the MNPs embedded in the PDMS matrix. The resulting photothermal heating results in heat diffusion from the MNPs to the surrounding breast tissue via the PDMS matrix. This raises the temperature of the surrounding residual tumor cells/healthy breast tissue above the normal body temperature of 37°C. In this way, the surrounding residual tumor cells are killed/inhibited.

In this study, the computational model explored the effects of laser illumination on water and the nanocomposite device, heat diffusion, and thermal damage on the breast tissue. The tumor was idealized as a sphere with a diameter of 2 cm. It was also assumed that the initial tumor was removed by lumpectomy. A spherical nanocomposite was inserted into the region of the removed tumor in the breast. The breast tissue was also modeled as a semi-ellipsoidal block with long and short axes diameters of 32 and 30 cm, respectively. The PDMs nanocomposite (implanted into the cavity in the breast tissue) was modeled using spherical geometries.

3.1 | Heat diffusion model

The heat diffusion equation is used to obtain the heat distribution within the device and surrounding media. The temperature distribution in solids, due to an external heat source, used in this work was determined from the Fourier heat conduction equation. The heat was assumed to be generated from the absorption of laser light. Hence, the governing equation is given by[46]:

$$\rho C_p \frac{\partial T}{\partial t} = \nabla \cdot \lambda \nabla T + Q \tag{2}$$

where, ρ $(\mathrm{kg\,m^{-3}})$ is the density, C_p $\left(\mathrm{J\,kg^{-1}\,K^{-1}}\right)$ is the specific heat capacity at constant pressure, λ $\left(\mathrm{W\,m^{-1}\,K^{-1}}\right)$ is the thermal conductivity, T (K) are temperature and Q $\left(\mathrm{W\,m^{-3}}\right)$ is the heat source term, which varies for the different domains of the model and is obtained using the linear superposition of multiple heat source terms. The heat sources in the nanocomposite domain, Q_{PNC} and tissue domain, Q_{tissue} are given by:

$$Q_{PNC} = \mu_a \varphi\left(\vec{r},t\right) N_T C_{abs} \varphi\left(\vec{r},t\right) \tag{3}$$

$$Q_{tissue} = \mu_a \varphi\left(\vec{r},t\right) \tag{4}$$

where, $\varphi\left(\vec{r},t\right)$ $\left(\mathrm{W\,m^{-2}}\right)$ is the laser light fluence rate, μ_a $\left(\mathrm{m^{-1}}\right)$ is the tissue, water, or polymer absorption coefficient, N_T is the total number of MNPs per unit volume and C_{abs} $\left(\mathrm{m^2}\right)$ is the absorption cross-section of MNP which is given as $C_{abs} = 4\pi r_o^2 Q_{abs}$[45] and r_o and Q_{abs} are the absorption efficiency and radius of the MNP, respectively. The laser light fluence rate of the optic fiber and the diffusion coefficient of the medium is defined as.[47]

$$\varphi\left(\vec{r},t\right) = \frac{P_o \exp\left(-\mu_{eff}\,\vec{r}\cdot\hat{n}\right)}{4\pi D r} \tag{5}$$

where, $\vec{r}$ is the position vector, P_0 is the laser power, and $\hat{n}$ is the normal vector showing the direction in which the laser beam travels. μ_{eff} and D are the effective attenuation coefficient and the diffusion coefficient of the medium, respectively, which are defined as:

$$\mu_{eff} = \sqrt{3\mu_a\left(\mu_a + \mu_s'\right)} \tag{6}$$

$$D = \frac{1}{3\left(\mu_s' + \mu_a\right)} \tag{7}$$

where, μ_a is the absorption coefficient and μ_s' is the reduced scattering coefficient, defined as:

$$\mu_s' = (1-g)\,\mu_s \tag{8}$$

where, μ_s is the scattering coefficient and g is the anisotropy factor, which accounts for the effects of directional dependent scattering. In this study, the parameters for PDMS and MNPs used are stated in Table 1.

15524981, 2022, 12, Downloaded from https://onlinelibrary.wiley.com/doi/10.1002/jbm.b.35124 by Egyptian National Sci. Network (Enstinet), Wiley Online Library on [08/11/2022]. See the Terms and Conditions (https://onlinelibrary.wiley.com/terms-and-conditions) on Wiley Online Library for rules of use; OA articles are governed by the applicable Creative Commons License

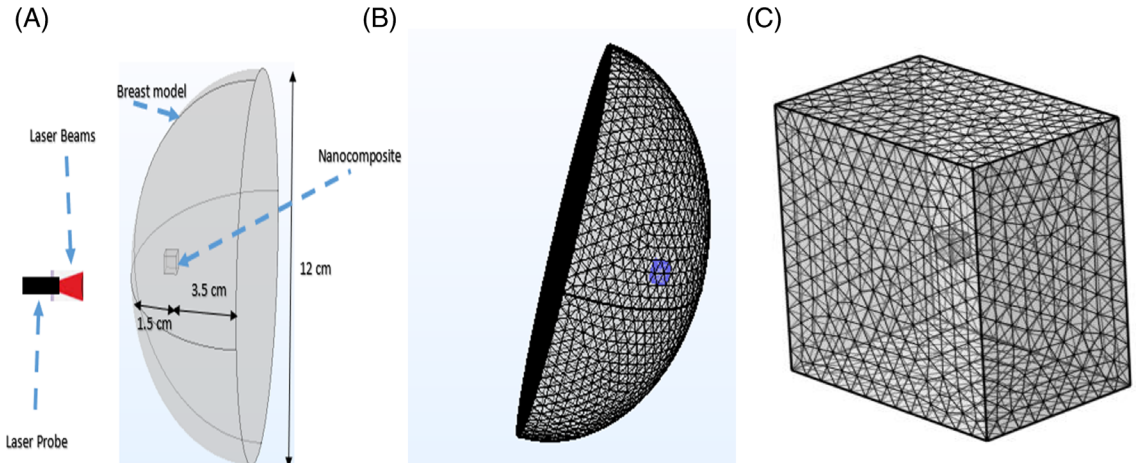


FIGURE 2 Schematic of a breast phantom with a long axis diameter of 12 cm and a short axis diameter of 5 cm. A 1 cm cubic cavity illustrates a region containing the nanocomposite, which is assumed to be located at 1.5 cm from the surface of the breast. The laser beam size is not drawn to scale. (B and C) Breast phantom mesh for FEM modeling

For biological media, the Pennes model[48] modifies Equation (2) by including the effects of heat generation due to constant blood perfusion, Q_p, and metabolic heat, Q_m. In this study, Q_p is defined as:

$$Q_p = \rho_b C_b \omega_b (T_b - T) \tag{9}$$

where, ρ_b, ω_b (s^{-1}), C_b and T_b are the density, blood perfusion rate, specific heat capacity, and temperature of blood, respectively. Q_m $(W\,m^{-3})$ is the metabolic heat, which is defined in Table 1.

The boundary conditions for Equation (2) in a breast phantom are heat transfer by convection between the top surface of the breast phantom and air, $\hat{n}\cdot(k\nabla T) = h\cdot(T_{ext} - T)$; where the heat transfer coefficient, $h = 3.5\,W\cdot m^{-1}\,K^{-1}$, $T_{ext} = 20^{\circ}C$; and continuity, $\hat{n}\cdot(\lambda_2\nabla T_2 - \lambda_1\nabla T_1) = 0$ on the internal boundaries. The initial temperature in all the domains of the model was set to the normal body temperature of 37°C.

The effective thermal and physical properties of the nanocomposites were estimated using the rule of mixture theories.[49] These give:

$$\rho = v_a\rho_a + (1 - v_a)\rho_b \tag{10}$$

$$k = \left(\frac{v_a}{k_a} + \frac{(1 - v_a)}{k_b}\right)^{-1} \tag{11}$$

where, subscripts "a" and "b" denote MNPs and PDMS matrix for the density, ρ, thermal conductivity, k, and specific heat capacity, C, values, respectively. Due to pronounced changes in blood perfusion, the thermal conductivity of living tissue can increase with increasing temperature.[50] The temperature-dependence of blood perfusion and thermal conductivity for breast tissue can be expressed as[51–55]:

$$V(T) = \omega_b \begin{cases} 1 + \exp\left(\dfrac{-(T - 45.0)^2}{12.0}\right) & \text{if } T \le 45.0^{\circ}C \\ 2, & \text{if } T > 45.0^{\circ}C \end{cases} \tag{12}$$

TABLE 2 Tissue parameters used for the simulations

Parameter	Value	Ref.
Tissue: Absorption coefficient, μ_a	2.2 m^{-1}	[47]
Tissue: Scattering coefficient, μ_s	12,200 m^{-1}	[47]
Tissue: Anisotropy constant, g	0.9	[47]
Tissue: Density, ρ	1000 kg m^{-3}	[47]
Tissue: Heat capacity, C_p	3400 J kg^{-1} K^{-1}	[47]
Tissue: Thermal conductivity, λ	0.587 W m^{-1} K^{-1}	[47]
Heat convection constant	3.5 W m^{-2} K^{-1}	[47]
Blood: Specific heat capacity, C_b	1080 kg m^{-3}	[83]
Blood: Density, ρ_b	1000 kg m^{-3}	[83]
Blood: Specific heat capacity, C_b	4200 J kg^{-1} K^{-1}	[83]
Blood: Perfusion rate	0.002 s^{-1}	[60]
Blood: Thermal conductivity, λ	0.39 W m^{-1} K^{-1}	[83]

$$k(T) = k_0[1 + 0.0028(T - 293.15\,K)] \tag{13}$$

where, k_0 is the thermal conductivity at 293.15 K. The values of all of the parameters that were used in the simulation are summarized in Table 1.

3.2 | Finite element modeling of temperature and thermal dose

Finally, in an effort to model the potential effects of actual breast geometries, a breast phantom model (Figure 2) was used to simulate the potential effects of laser illumination on breast-like geometries. The schematic in Figure 2 shows a model with a long axis diameter of 12 cm and a short axis diameter of 5 cm. A 1 cm cubic cavity was

15524981, 2022, 12, Downloaded from https://onlinelibrary.wiley.com/doi/10.1002/jbm.b.35124 by Egyptian National Sci. Network (Enstine), Wiley Online Library on [08/11/2022]. See the Terms and Conditions (https://onlinelibrary.wiley.com/terms-and-conditions) on Wiley Online Library for rules of use; OA articles are governed by the applicable Creative Commons License

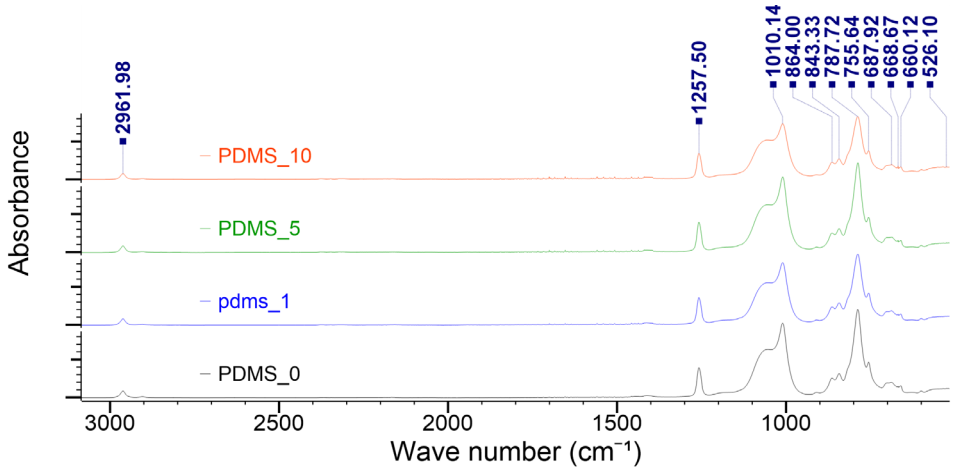


FIGURE 3 Fourier-transform infrared spectra of plain PDMS and PDMS nanocomposites with varying weight fractions (1%, 5%, and 10%) of magnetite nanoparticles

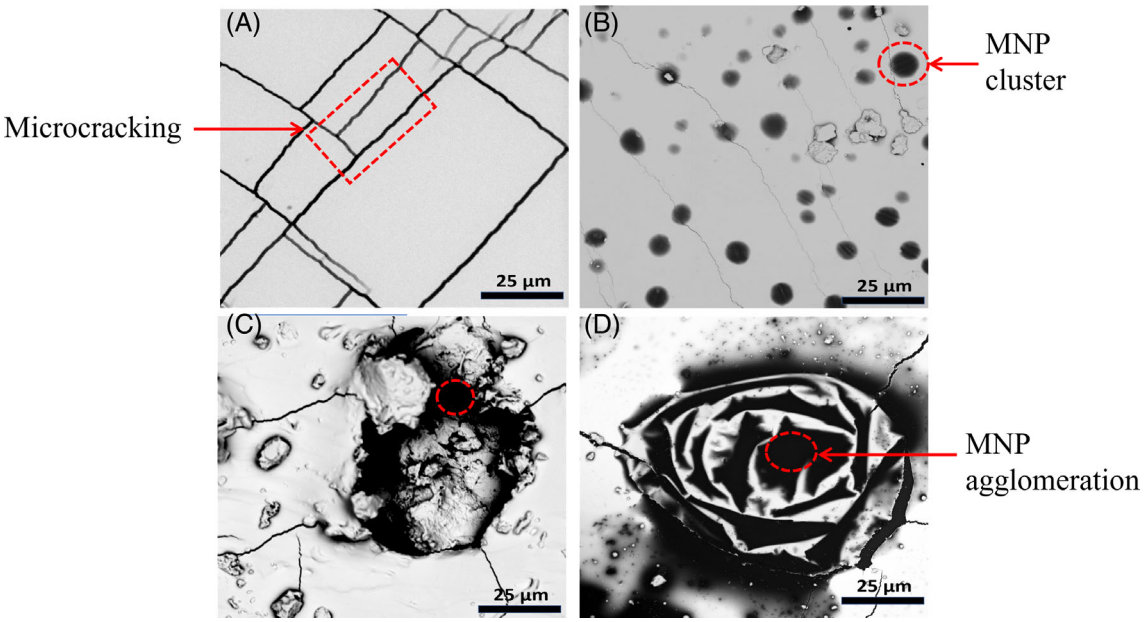


FIGURE 4 Backscattered SEM images of (A) plain PDMS, (B) PDMS_1% MNP, (C) PDMS_5% MNP, and (D) PDMS_10% MNP

inserted to enable the insertion of the PDMS nanocomposite structures at a distance of 1.5 cm from the surface of the breast. The concentration of the MNPs in the PDMS nanocomposite devices 10^{-5} MNPs/ml was used to control the maximum temperature that was reached after the 30 min of laser illumination.

The temperature profile is generally used to describe the size of lesions predicted by numerical models.[56] However, in many cases, the temperature does not correlate well with histological measurements from actual tissue.[56] Hence, several investigators[57–61] have used the concept of a "thermal dose" to assess the relative effectiveness of tumor hyperthermia treatment. In this study, we used a method developed by Sapereto et al.,[62] which describes protein inactivation rate at different temperature and time intervals, thereby expressing the thermal dose as a cumulative equivalent minute of exposure at 43°C (CEM_{43}) using the formula:

$$CEM_{43} = \int_0^{t_f} R^{[43-T(t)]} dt \quad (14)$$

where, t_f is the treatment duration and R is the factor to compensate for a 1°C temperature change. This has a value of 0.233 when the temperature as a function of time $T(t)$ represents the actual applied temperature of the target tissue, which is less than 43 °C or 0.428 otherwise.[63]

To numerically study the effect of MNPs on the heat absorption behavior of the nanocomposite structures, finite element analyses (FEA) of pure PDMS and nanocomposite with 5% MNPs were performed using the commercial software Abaqus for different laser powers. Assuming that the scattering process dominates absorption, the optical diffusion approximation can be used to obtain the light fluence rate $\varphi(\vec{r})\left(\frac{W}{m^2}\right)$ within the device for a continuous wave

15524981, 2022, 12, Downloaded from https://onlinelibrary.wiley.com/doi/10.1002/jbm.b.35124 by Egyptian National Sci. Network (Enstinet), Wiley Online Library on [08/11/2022]. See the Terms and Conditions (https://onlinelibrary.wiley.com/terms-and-conditions) on Wiley Online Library for rules of use; OA articles are governed by the applicable Creative Commons License

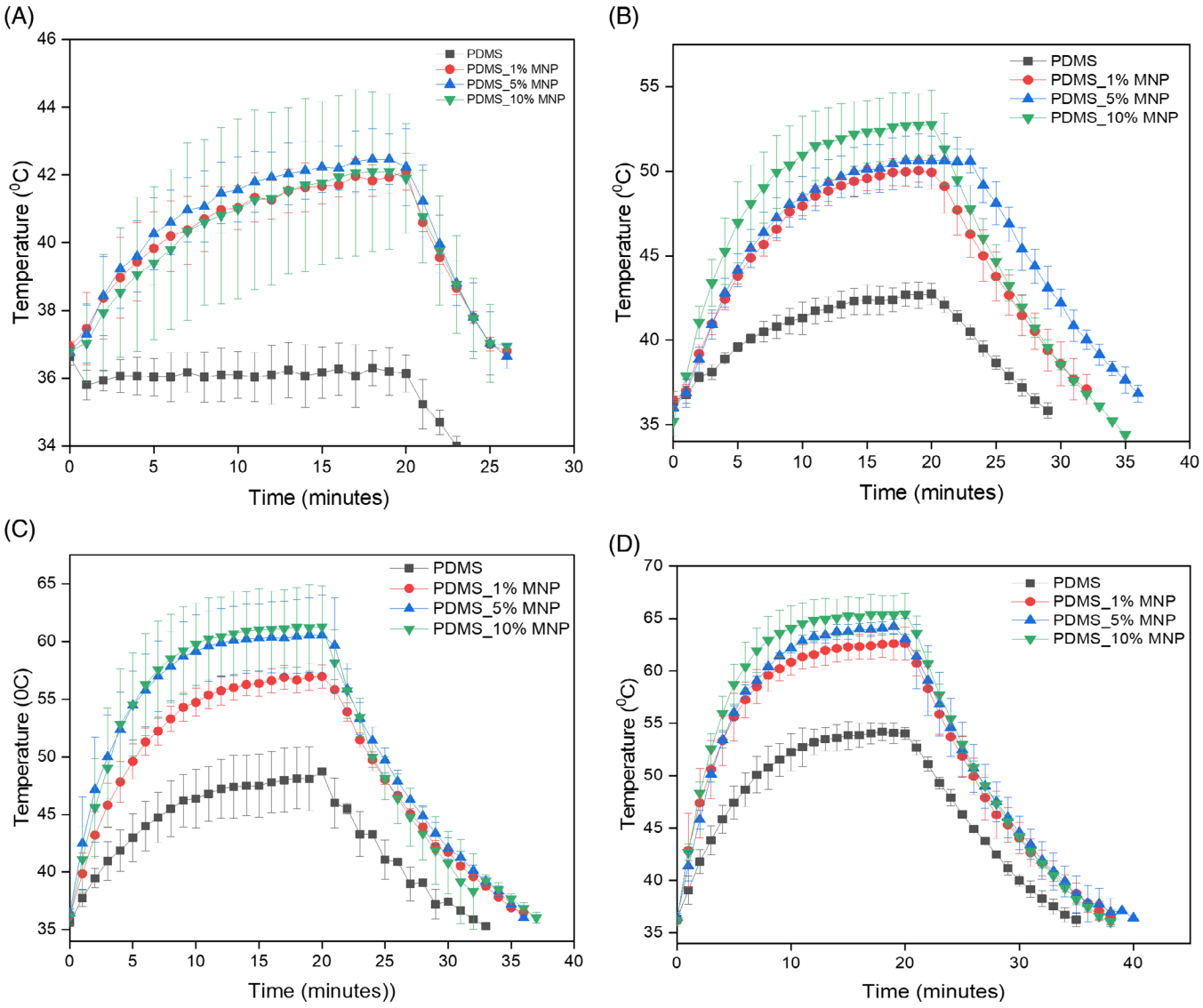


FIGURE 5 Plots of temperature as a function of time at laser powers of (A) 0.6 W, (B) 1.0 W (C), 1.5 W, and (D) 2.0 W for PDMS nanocomposites with 0%, 1%, 5%, and 10% MNPs in water

Gaussian laser beam.[47] 3D models of the cubic device and media with the dimension of 0.5 and 2 cm, respectively, were built in Abaqus. Standard 8 node linear heat transfer elements were used to mesh the geometry.

Heat convention is modeled by applying surface film condition with film coefficient equal to 30 $\left(\frac{W}{m^2 K}\right)$ and uniform sink temperature equal to 25°C to the boundaries of the media. This value is chosen in a way that the best agreement between the numerical and experimental results is achieved. For simplicity, the heat convection coefficient is considered constant and similar for all sides of the boundary. As the temperature increases, steam exits from the cuvette, and heat loss will increase from the top side and will cause a deviation in the predicted numerical results with respect to the experimental results. The initial temperature of the device and the media is considered to be 37°C. The transient heat transfer step is applied to solve the problem. Total analysis time is considered to be 30 min. The laser heat source is applied for the beginning 20 min and removed for the remaining 10 min of the analysis. The model is run for laser powers of 0.5, 0.6, 1.0, 1.5, and 2 W for pure PDMS and nanocomposite with 5% MNPs.

The in vivo predictions of the temperature profile on the breast phantom and thermal damage were also obtained using a commercial FEM package (COMSOL Multiphysics 5.5, COMSOL, Inc., Burlington, MA). The geometrical model that was used in our study is shown schematically in Figure 2. This is similar to that used by Reynoso et al.[47] for modeling gold nanoparticle-mediated heating. The device was assumed to be inserted into the breast tissue within a cavity created after the tumor is surgically removed, which was modeled as a semi-ellipsoidal block with 12 and 6 cm major and minor axis, respectively (Figure 2A,B). The total analysis time of 35 min consisted of 30 min of heating and 5 min of cooling. The simulations were carried out for laser powers of 0.6 W and PDMS nanocomposites with 5% of MNPs. Similar approaches were also used to predict the temperatures and the thermal dose/damage associated with the model experiments in the chicken tissue. The parameters of the tissue that were used for the simulations are summarized in Table 2.

15524981, 2022, 12, Downloaded from https://onlinelibrary.wiley.com/doi/10.1002/jbm.b.35124 by Egyptian National Sci. Network (Enstinet), Wiley Online Library on [08/11/2022]. See the Terms and Conditions (https://onlinelibrary.wiley.com/terms-and-conditions) on Wiley Online Library for rules of use; OA articles are governed by the applicable Creative Commons License

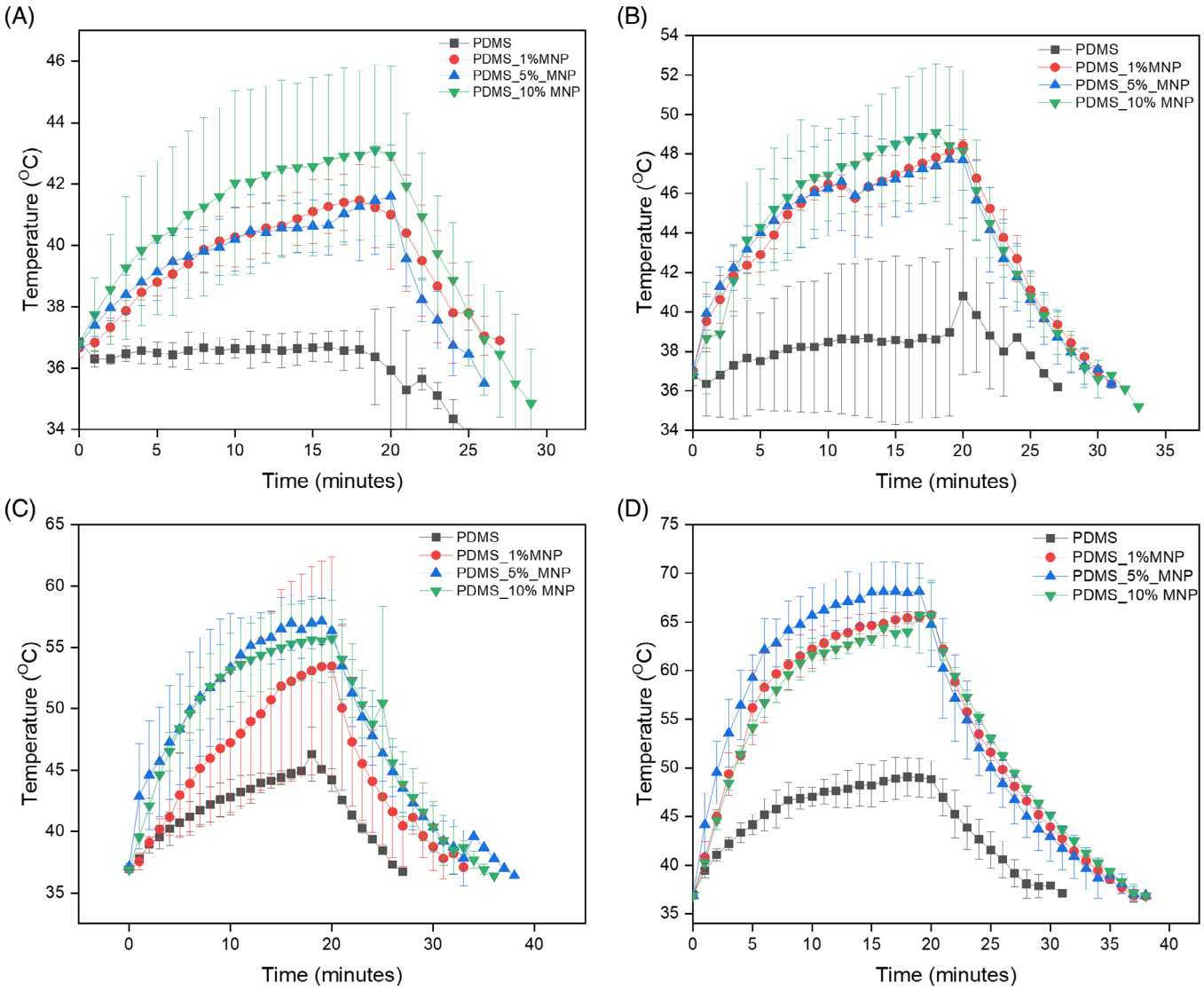


FIGURE 6 Plots of temperature as a function of time at laser powers of (A) 0.6 W, (B) 1.0 W, (C) 1.5 W, and (D) 2.0 W for PDMS nanocomposites with 0%, 1%, 5%, and 10% MNPs in L15+ culture medium

4 | RESULTS

4.1 | Physicochemical properties of the PDMS-magnetite nanocomposites

The FTIR spectra obtained for the plain PDMS and PDMS-MNP nanocomposites are presented in Figure 3. The spectra exhibited peaks at 787 cm^{-1} associated with —CH_3 rocking and Si—C stretching in Si—CH_3 and at 1010 cm^{-1} due to Si—O—Si stretching. There were also peaks at 1275 and 2962 cm^{-1} corresponding to CH_3 deformation in Si—CH_3 and asymmetric CH_3 stretching in Si—CH_3, respectively.[64] MNP signature corresponds to 668–526 cm^{-1} peaks.

Figure 4 shows backscattered SEM micrographs of the PDMS-MNP nanocomposites that were obtained to gain an insight into the nanoparticle distribution within the PDMS nanocomposites. The results show the dispersion of MNPs and magnetite nanoclusters within the PDMS matrix (Figure 4). The microstructure of the three PDMS nanocomposites (1%, 5%, and 10% MNP) show non-homogeneous distributions of the nanoparticles. Nanoparticle agglomeration was observed in the PDMS nanocomposites reinforced with 5% and 10% weight fractions of MNPs. Some evidence of microcracking in the PDMS matrix was also observed, with the incidence of microcracking increasing with increasing weight fraction. These results show that the nanoparticles were not well dispersed throughout the polymer matrix.

4.2 | Photothermal properties of the PDMS-magnetite nanocomposites

Figure 5 shows the temperature changes that occurred during the heating and cooling PDMS-MNP nanocomposites in water. With the exception of plain PDMS, the temperatures generally increased

15524981, 2022, 12, Downloaded from https://onlinelibrary.wiley.com/doi/10.1002/jbm.b.35124 by Egyptian National Sci. Network (Enstinet), Wiley Online Library on [08/11/2022]. See the Terms and Conditions (https://onlinelibrary.wiley.com/terms-and-conditions) on Wiley Online Library for rules of use; OA articles are governed by the applicable Creative Commons License

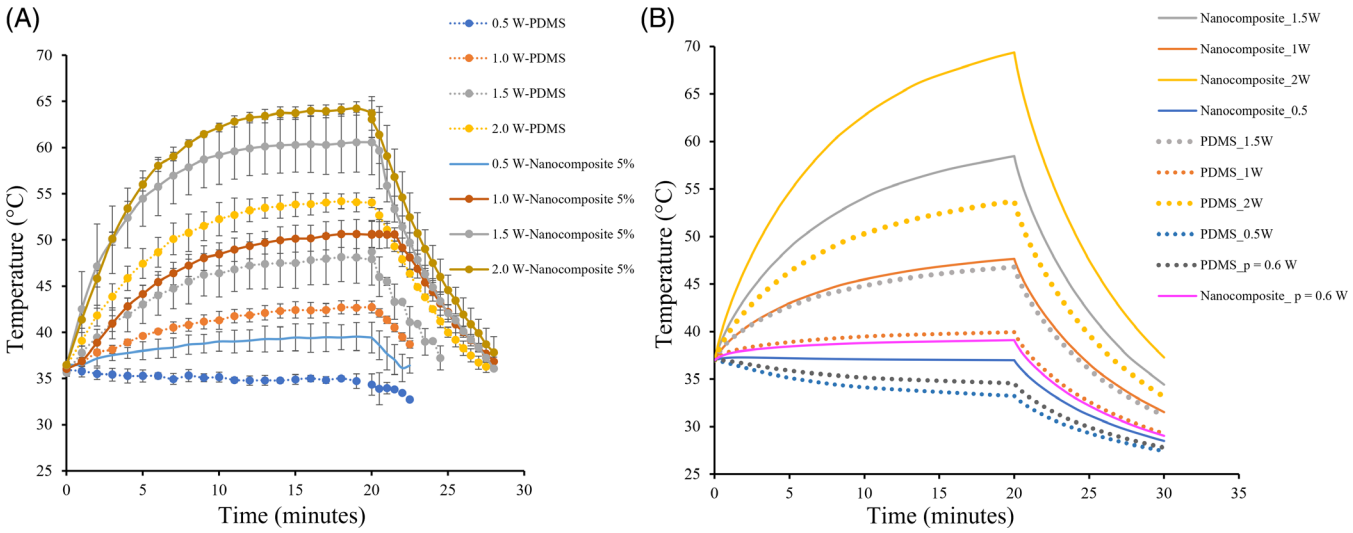


FIGURE 7 Comparison of (A) experimental data with (B) numerical predictions of the temperature profiles of the PDMS and PDMS-MNP nanocomposite devices in water at different laser powers

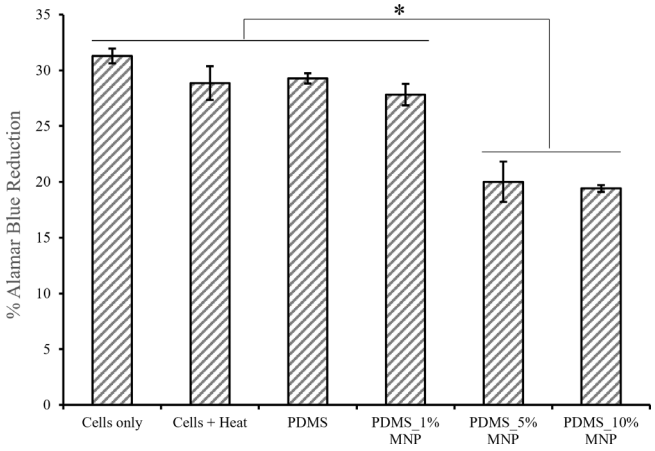


FIGURE 8 Effects of laser heating of the PDMS-MNP nanocomposites at 0.6 W for 30 min on the viability of MDA-MD-231 triple-negative breast cancer cells as measured by the percentage alamar blue reduction. Error bars represent the standard deviation for $n = 3$. $^*p < .05$

with increasing duration of laser/material interactions. The photothermally-induced temperature rise also increased with increasing laser power between 0.6 and 2.0 W after 20 min of laser irradiation. At low laser powers (0.6 W), the interactions of the laser light with the MNPs did not generate sufficient heat to distinguish between the different weight fractions of MNPs in the nanocomposites. However, the differences in the MNP content were generally observed at increased laser powers where the laser/MNP interactions generate heat relative to the amount of nanoparticles present in the nanocomposites.

Laser illumination with a power of 0.6 W resulted in maximum temperatures that were largely in the hyperthermic domain (41–44°C) for the polymer nanocomposite samples, while laser powers of 1.5 and 2.0 W gave rise to maximum temperatures far above the hyperthermia domain (in the so called "necrotic/ablation" domain). After turning off the incident laser beam following 20 min of heating, the nanocomposites and the surrounding liquid medium generally cooled rapidly (within 6 min) back to 37°C.

The changes in temperature induced by laser/nanocomposite interactions in the L15+ medium are presented in Figure 6A–F. The trends in the temperature profiles were similar to those presented for the PDMS-MNP nanocomposites immersed in water (Figure 5). However, the magnitudes of the temperature changes were somewhat different due to differences in the thermal properties of the water and the L15+ medium.

4.3 | Comparisons of temperature measurements with predictions of temperature profiles in water

A comparison of the measured and predicted temperature changes obtained from the magnetite-reinforced PDMS nanocomposites reinforced with 5 wt% of magnetite is presented in Figure 7A,B for composites immersed in water. The measured temperatures of the magnetite reinforced PDMS nanocomposites increased with increasing laser power for composites reinforced with 5 wt% of MNPs. The measured temperatures also decreased with increasing time, upon the removal of the incident laser illumination. Furthermore, the trends in the measured and predicted temperature changes were very similar during the heating and cooling stages. This is shown in Figure 7B in which the predictions from the finite element model are compared with the temperature measurements obtained from the computational modeling. This has been reported previously in our work.[59]

15524981, 2022, 12, Downloaded from https://onlinelibrary.wiley.com/doi/10.1002/jbm.b.35124 by Egyptian National Sci. Network (Enstinet), Wiley Online Library on [08/11/2022]. See the Terms and Conditions (https://onlinelibrary.wiley.com/terms-and-conditions) on Wiley Online Library for rules of use; OA articles are governed by the applicable Creative Commons License

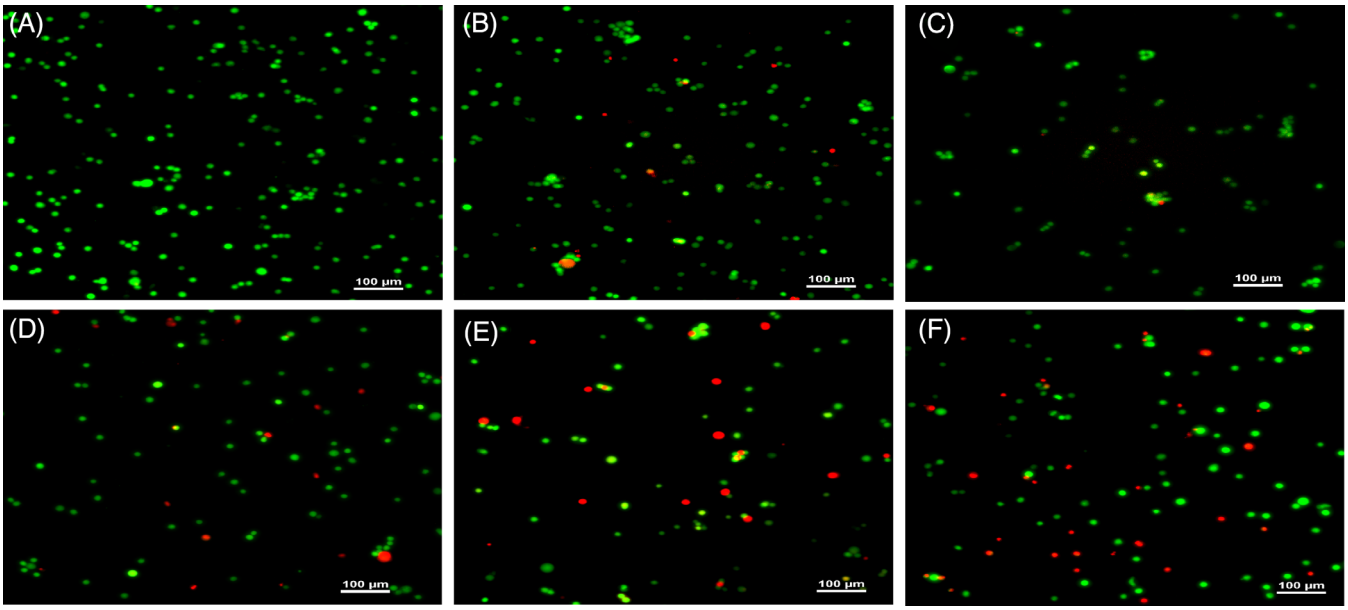


FIGURE 9 Fluorescence images of live (green) and dead (red) MDA-MB-231 cells after exposure to (A) MDA-MB-231 cells (no laser heating, negative control), (B) MDA-MB-231 cells, (C) plain PDMS, (D) PDMS_1% MNP, (E) PDMS_5% MNP, and (F) PDMS_10% MNP subjected to laser heating at 0.6 W for 30 min

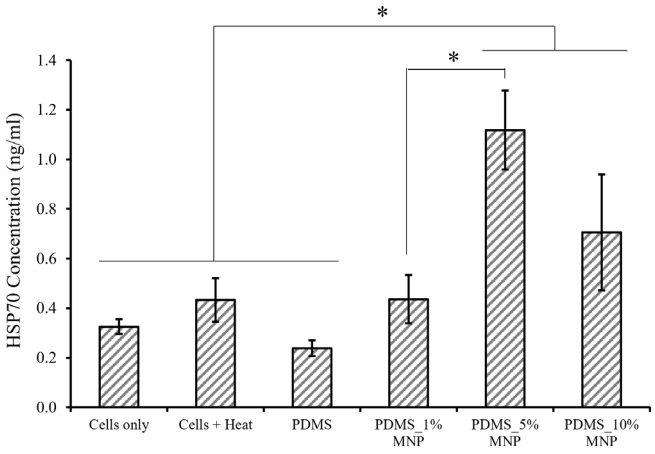


FIGURE 10 A plot of the amount of heat shock proteins released from stressed cells due to laser heating of the nanocomposites at 0.6 W. Error bars represent the standard deviation for $n = 3$. $^*p < .05$

4.4 | Effects of laser-induced heating in L15+ medium on cell viability

The studies in the L15+ medium also enabled us to study the effects of the laser-induced temperature changes of the cell viability. The results of the alamar blue assay study are presented in Figure 8. The percentage alamar blue reduction was plotted against the weight fraction with two controls (cells only and cells + heat). The results show that there is a significant reduction in cell viability compared with the cell only controls (by about 35%) in the case of hyperthermic heating due to laser interactions with PDMS nanocomposites reinforced with 5 or 10 wt% MNPs. However, there was no significant reduction in the case of laser interactions with pure PDMS or PDMS reinforced with 1 wt% of MNPs.

Live/death staining was done to visualize the quantitative view of life and death cells as shown in the cell viability (Figure 8). This is seen in Figure 9 as more cell deaths are seen where there is a significant reduction of alamar blue (5% and 10%) as presented above.

Further evidence of the effects of heat is also apparent from the detection of heat shock proteins (HSPs) resulting from stress-induced cell death due to the localized heating around the nanocomposites. The results of the heat shock protein assay are presented in Figure 10. The heat associated with hyperthermia induces heat stress on tumor cells, which causes the release of heat shock protein as earlier reported.[65,66] This suggests that the decrease in cell viability observed above after localized heating (Figure 8) can be attributed to the effects of heat stress/shock due to increased HSP expression that results in a decrease in cell viability.

4.5 | Chicken model

Beyond the in vitro experiments discussed above, a chicken model was used to mimic the tissue laser interactions that can occur during potential in vivo applications of the magnetic nanocomposites in localized hyperthermia. The measured temperature changes are presented in Figure 11A–C for measurements that were obtained at depths of 2 and 8 mm beneath the skin. The results show that laser penetration into the tissue was significant at both penetration depths. This was true for the range of laser powers that was explored in this study (0.5–3 W). However, in the case of the composites inserted at depths of 8 mm, only the 3 W laser power was sufficient to heat up to the

15524981, 2022, 12, Downloaded from https://onlinelibrary.wiley.com/doi/10.1002/jbm.b.35124 by Egyptian National Sci. Network (Enstine), Wiley Online Library on [08/11/2022]. See the Terms and Conditions (https://onlinelibrary.wiley.com/terms-and-conditions) on Wiley Online Library for rules of use; OA articles are governed by the applicable Creative Commons License

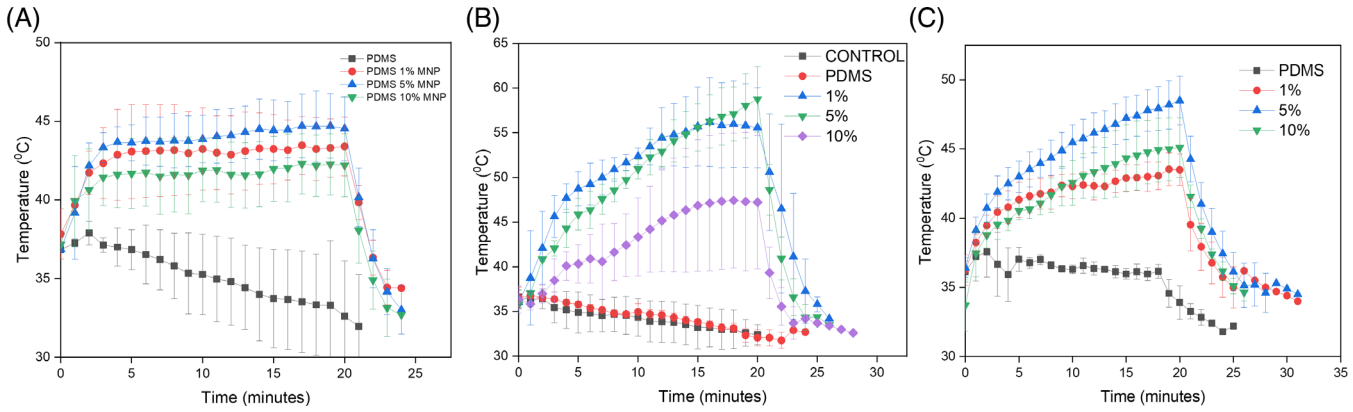


FIGURE 11 Measured temperature profiles around nanocomposite devices in chicken models inserted at: (A) 2 mm depth and heated with 0.6 W of laser power; (B) 2 mm depth and heated with 1.0 W of laser power, and (C) 8 mm depth heated with 3.0 W of laser power

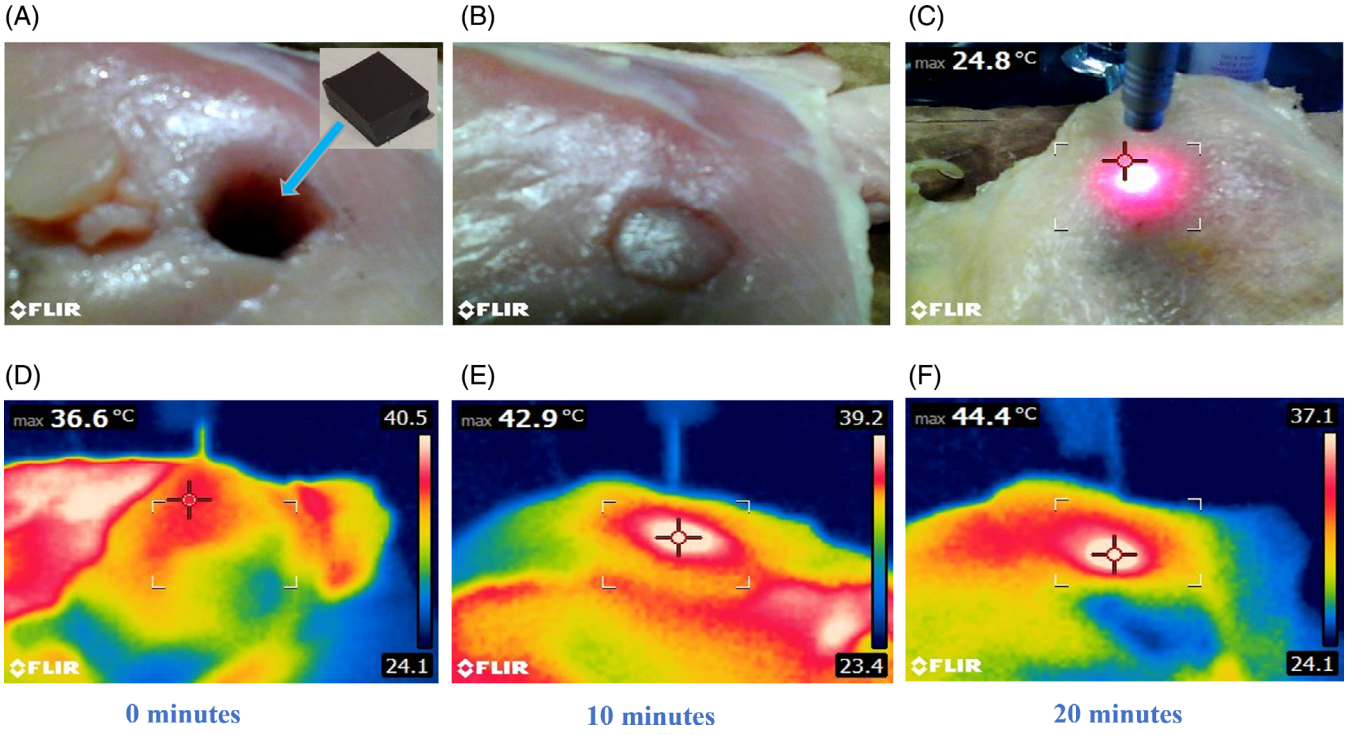


FIGURE 12 Processing of the chicken sample used for the chicken model experiments: (A) 1 cm diameter × 8 mm depth groove dissected for burying the nanocomposite devices, (B) the buried device covered with the dissected chicken tissue from the groove, and (C) the groove covered with chicken skin and the laser illuminated on the device underneath the skin. IR thermal images of the surface of the chicken skin are also displayed after (D) 0 min, (E) 10 min, and (F) 20 min of laser-induced heating of the devices buried in the chicken tissue at 8 mm depths

hyperthermic regime (41–44°C). However, in the case of composites immersed at depths of 2 mm, significant heating was achieved at laser powers of 0.6 and 1.0 W. It is interesting to note here that the 0.6 W of incident laser power resulted in hyperthermic heating, while 1.0 W of incident laser power and more resulted in temperature changes that are sufficient for photoablation.[41] We found that when the depth was increased, an interplay between laser power and MNP content determined the heating level obtained. To obtain hyperthermic temperatures, either laser power or MNP content or both had to increase as the depth increased. Therefore, if a tumor is more than 8 mm deep, the laser power or the MNP content of the nanocomposite or both can be increased (within safe levels) to generate hyperthermic temperatures to inhibit cancer cell growth.

The spatial and temporal variations associated with the laser/material interactions with the magnetite reinforced PDMS nanocomposites embedded in chicken tissue are presented in Figure 12. These show increasing temperature profiles with increasing laser power. The results also show that the temperature at the centers of the nanocomposites and the tissue interface increase with increasing heating durations of up to 30 min.

15524981, 2022, 12, Downloaded from https://onlinelibrary.wiley.com/doi/10.1002/jbm.b.35124 by Egyptian National Sci. Network (Enstinet), Wiley Online Library on [08/11/2022]. See the Terms and Conditions (https://onlinelibrary.wiley.com/terms-and-conditions) on Wiley Online Library for rules of use; OA articles are governed by the applicable Creative Commons License

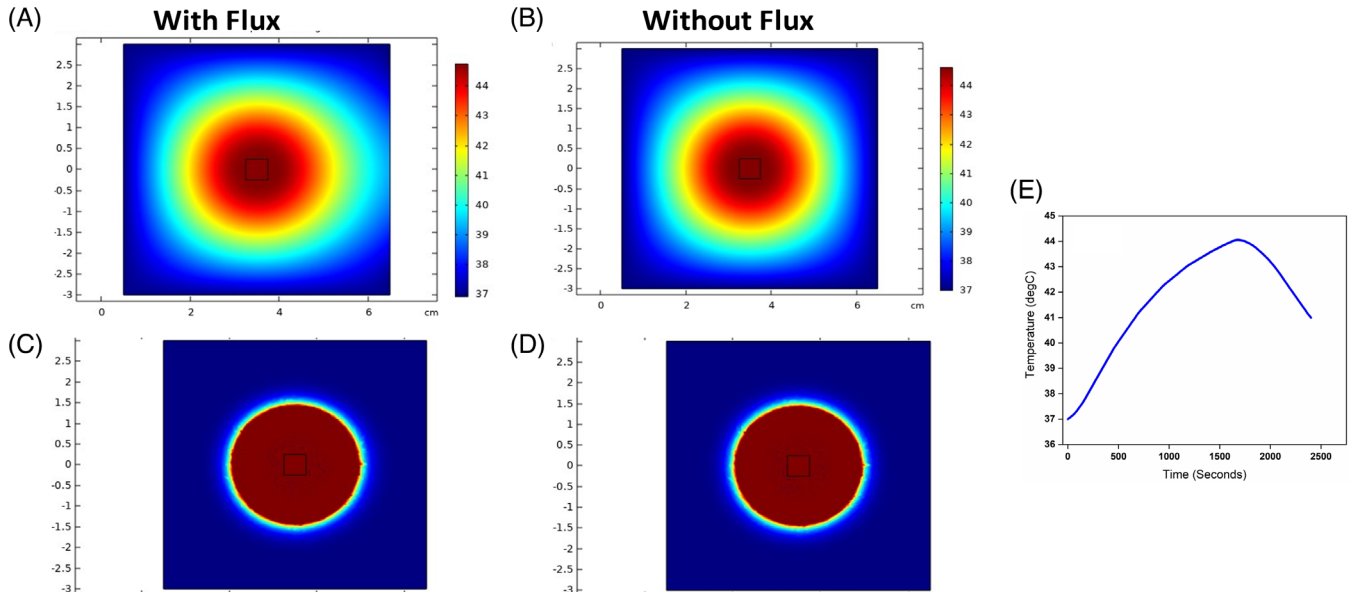


FIGURE 13 FEM cross-sectional view of the chicken model showing temperature changes after 30 min of 0.6 W NIR laser illumination (A) 2D plot of temperature versus time for the Chicken model prediction with flux; (B) 2D plot of temperature versus time for the Chicken model prediction without flux; (C) cross-sectional (*x*–*y*) view of the thermal damage when chicken tissue is subjected to 30 min of 0.6 W of NIR laser illumination, and (D) cross-sectional view of thermal damage after 30 min of laser heating under 0.6 W NIR laser illumination and 5 min of cooling

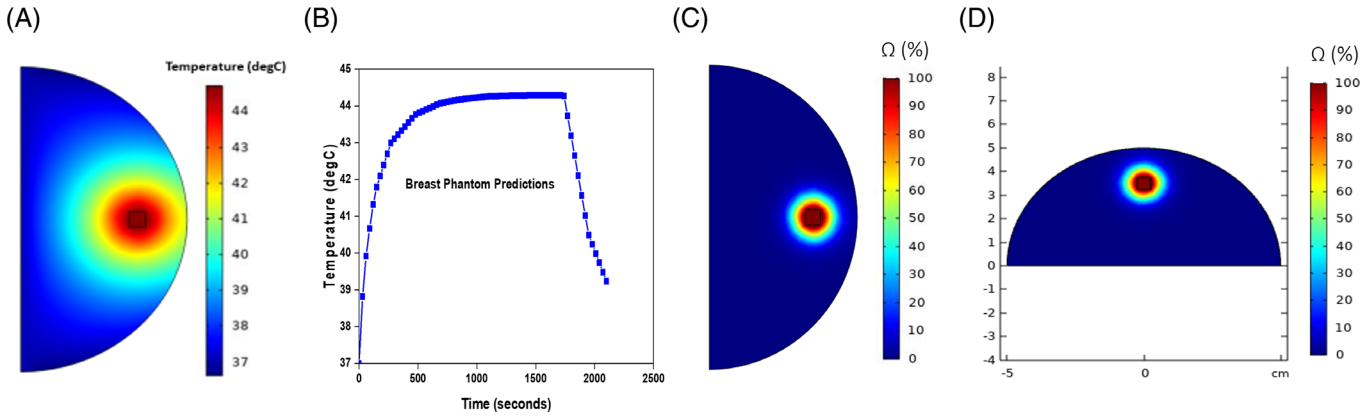


FIGURE 14 (A) FEM cross-sectional view of a breast phantom showing temperature changes after 30 min of 0.6 W NIR laser illumination; (B) a plot of temperature versus time for the breast phantom prediction; and cross-sectional (*x*–*y*) views of the thermal damage when breast tissue is subjected to (C) 30 min of 0.6 W NIR laser illumination, and (D) 30 min heating and 5 min cooling

However, the temperature distribution is non-uniformly distributed, with the maximum temperatures occurring within the devices. The heat also spreads radially outwards into the surrounding tissue (Figure 12D–F), while the maximum tissue temperature occurs at the interface between the device surfaces and the chicken tissue. In the case of nanocomposite devices exposed to incident laser power of 0.6 W, the predicted maximum temperature was 44°C, which is within the hyperthermic regime, and in agreement with the experimental results. Similarly, the predicted cooling temperatures (after turning off the laser/materials heat source) are comparable to the experimental results (Figure 12).

We observed from the chicken experiments that the NIR laser did not physically damage the chicken tissue while penetrating through it to interact with the MNPs in the PDMS matrix buried in the chicken tissue. No heating effects were also observed from the interaction between the NIR laser beam and the plain PDMS. This is in agreement with the reports in the literature that heating cancer/tissue with NIR laser is non-invasive.[67]

Finally, in this section, it is of interest to note that significant cooling occurred rapidly, upon the removal of heat flux due to the incident laser beam. The measured temperature distributions are in the ranges that are sufficient for localized hyperthermia (41–44°C) when the incident laser power is 0.6 W. Above this, the induced

15524981, 2022, 12, Downloaded from https://onlinelibrary.wiley.com/doi/10.1002/jbm.b.35124 by Egyptian National Sci. Network (Enstinet), Wiley Online Library on [08/11/2022]. See the Terms and Conditions (https://onlinelibrary.wiley.com/terms-and-conditions) on Wiley Online Library for rules of use; OA articles are governed by the applicable Creative Commons License

temperature variations are in ranges that are suitable for tissue necrosis and ablation.[41]

4.6 | In vivo prediction of temperature profile and tissue damage

The corresponding cross-sectional views of the temperature distributions (Figure 13A,B) and thermal damage (Figure 13C,D) associated with the heating and cooling stages of the chicken models suggest that the thermal doses are sufficient for the hyperthermic treatment of tissue. Similarly, in the case of the human tissue in vivo simulations (Figure 2), the corresponding lesions predicted for scenarios corresponding to 30 min of heating at 43°C (surface temperature) with cubic MNP-reinforced PDMS structures presented in Figure 14, for laser-induced heating and after the removal of laser-induced heating.

The finite element results show that the temperature distribution is non-uniform, with the highest temperatures occurring at the center of the tissue. The resulting shape of the lesion is also slightly irregular (Figure 14A,D). The predictions show that the lesion sizes increase mostly around the device. This means that the residual tumor cells, which are assumed to be close to the heated device, experience higher temperatures than the healthy cell/tissues.

5 | DISCUSSION

The results of the physicochemical properties show that the bands were well maintained for the PDMS samples, irrespective of the weight percentage of MNPs. While the tetrahedral and octahedral sites for Fe-0 are maintained.[68] Thus, no primary chemical bonds were formed during the fabrication process and the PDMS-MNP nanocomposites were simply pure mixtures of PDMS and MNPs.

SEM micrographs of the PDMS-MNP nanocomposites presented also show the dispersion of MNPs and magnetite nanoclusters within the PDMS matrix, which is in agreement with our results earlier reported.[69] The distribution of MNPs within the nanocomposites was not homogeneous and agglomeration was observed in the 5% and 10% MNP nanocomposites (Figure 5). It is important to note that the nanoparticles agglomerate due increased packing density (decreasing distance between the nanoparticles).[70] The ideal situation was considered in the simulations where the nanoparticles were assumed to be homogenously dispersed within the PDMS matrix. The temperature versus time predictions from the simulations were compared with the experimental data where there is non-homogeneous dispersion and both results followed the same trend, as shown in Figure 7.

The photothermal properties of the PDMS-magnetite nanocomposites immersed in water and L15+ medium at different laser power for both heating and cooling shows that the temperature increases with the increasing duration of laser/material interaction as earlier reported[23,65] and with increase in power. Laser-induced heating in water and L15+ medium resulted in significant increases in the temperatures of the nanocomposites compared to the plain PDMS ($p < .05$). However, there were no significant differences ($p > .05$) among the nanocomposite samples, although temperature increases were observed between the 1, 5, and 10 wt% MNP samples. Although in the case of laser-induced heating in L15+ medium at 2.0 W. The temperature increase for the 5 wt% MNP samples were higher than their 10 wt% MNP counterparts. This was probably the result of the agglomeration of MNPs at higher nanoparticle weight percentages, which caused magnetic attractions and weak dipole–dipole interactions as a result of van der Waals forces.[70] The comparison of the measured and predicted temperature changes of the nanocomposite device in water shows the same trend.[59]

This photothermal properties mentioned above depends solely on the principle of laser heating of the MNP nanocomposites. The unique interaction of MNP with light comes from SPR, that is, the resonance oscillation of free electrons in the magnetite with light. This interaction leads to a number of phenomena—thermal, optical, electrical in and around the magnetite. When the laser is irradiated to the nanoparticles, light/electromagnetic radiation interacts with plasmonic nanoparticles, the oscillating magnetic fields from the radiation causes the oscillations of the conduction band electrons around the surface of the nanoparticles. This oscillation causes heat production.[71–73]

Temperature rise depends on the photothermal conversion efficiency of the photothermal agent, the concentration of nanoparticle and the dosage of light delivered.[74] Initially, the deposited laser power was not enough to enrich dissociation of water. The dissociation and ionization reaction were conspicuous which is shown in the temperature rise. Beyond a laser power of 0.6 W the temperature increases gradually. Initially, the temperature rose slowly (due to lower power) and increased up to a laser power of 2 W. Another factor that affected the temperature rise was the photodissociation time. It is perceived that the temperature rise follows a stepwise time pattern as seen in Figures 5–7.

At higher laser powers, higher temperature rise occurred in shorter durations. Hence, in such cases higher temperatures were reached within 5 min, while steady state temperatures occurred within 10–20 min of higher power illumination. However, at lower power, longer duration of laser illumination was needed to reach the steady state temperature.

In general, when the temperatures associated with the lower power (~0.6 W) were in the hyperthermic regime (41–44°C) in which programmed cell death (apoptosis) was associated with laser illumination. On the other hand, if the electromagnetic radiation has a resonant frequency matching these oscillations, the interaction between radiation and nanoparticle is extremely intense.[71] The heat associated with hyperthermia induces heat stress on tumor cells, which causes the release of heat shock protein as earlier reported.[65,66] This suggests that the decrease in cell viability observed above after localized heating (Figure 8) can be attributed to the effects of programmed cell death due to increased HSP expression that results in a decrease in cell viability. The implications of the current work are quite significant for the design of cancer treatment conditions, the use of implantable magnetite nanocomposite for heat generation through near-infrared laser illumination. The result suggests that by controlling the

15524981, 2022, 12, Downloaded from https://onlinelibrary.wiley.com/doi/10.1002/jbm.b.35124 by Egyptian National Sci. Network (Enstinet), Wiley Online Library on [08/11/2022]. See the Terms and Conditions (https://onlinelibrary.wiley.com/terms-and-conditions) on Wiley Online Library for rules of use; OA articles are governed by the applicable Creative Commons License

parameters such as the magnetite concentration, laser power, and treatment time, this device can be designed to generate the heat that is needed to kill cancer cells. The device can be implanted into cavities that are created after the surgical removal of tumors[75] to take care of the residual cancer cells and facilitate the postoperative treatment of cancer. This approach can also be used effectively to measure temperature changes observed for different laser power intensities that can optimize the control of programmed cell death.

The type of laser applied in many photothermal investigations was near infrared, with wavelength spectra of 785 nm up to 1046 nm, with 808 nm wavelength used more frequently, according to a review by Fekrazad et al.[76] Hence, the 808 nm wavelength was the most effective in prior studies[77–79] of the photothermal destruction of cancer cells.[76]

In addition, the current results suggest that the magnetite-reinforced PDMS nanocomposites reinforced with 5% weight percentage of MNPs exhibit the best heating characteristics for controlled laser-induced hyperthermia at depths up to 8 mm below the surface, when the power of the incident laser is 0.6 W. However, for laser power above 0.6 W, the current work also suggests that the higher temperatures that result from laser illumination at higher incident powers (above 0.6 W). Within this context, laser powers of 1.5 W and above can be used to induce much higher temperatures that are sufficient to ablate tissue in ways that could enable the future development of laser scalpels. However, further work is needed to demonstrate the feasibility of such concepts under in vitro and in vivo conditions.

Finally, it is of interest to note that the positioning and movement of the laser can be managed by a robotically-assisted positioning device. Hence, the insights from the current work can be integrated into a robotically assisted laser positioning system that can be used to guide laser beams with well controlled power and wavelengths to interact with MNPs to induce heating that is sufficient to enable photothermal therapy via laser hyperthermia. The current chicken experiments demonstrate that sufficient hyperthermic heating can be engineered in chicken tissues at depths of 8 mm beneath the skin surface. Higher temperatures may also be induced at higher laser powers, which may be useful in future robotically-assisted surgical procedures.

6 | CONCLUSIONS

The paper presents the results of a combined experimental and analytical/computational study of the effects of laser interactions on the heating in nanocomposites that consist of MNPs in a matrix of PDMS. The magnitude of the heating also increases significantly with increasing laser power and MNP weight percentages between 1 and 5 wt%. However, above this weight percentage, increasing MNP weight percentage does not necessarily result in increased heating. In the case of PDMS reinforced with 5 wt% of magnetite, and exposed to 0.6 W of incident laser power, the induced increase in temperature is associated with a reduction of cell viability in triple-negative breast cancer cells that are heated to temperatures in the hyperthermic regime (41–44°C). Above this, the decrease in cell viability is attributed to necrosis, as the induced temperatures range between 45 and 70°C. The induced heating in the regions surrounding the nanocomposite structures are well predicted by computational models of heating (during exposure of MNPs to laser beams) and cooling (upon removal of the incident laser beams). The results from the chicken experiments also showed that the near-infrared laser we used did not cause physical damage to the chicken tissue but penetrated the tissue and interacted directly with the MNPs in the PDMS matrix. The above results suggest that PDMS nanocomposite structures can be used as thermoseeds for the localized heating and treatment of breast tumors. Animal work and clinical trials are clearly needed to explore the characteristics of these PDMS nanocomposites for possible applications in localized hyperthermia and laser surgery.

ACKNOWLEDGMENTS

This work was supported by the Pan African Material Research Institute (PAMI) with funding from the World Bank African Centers of Excellence (ACE) (Grant No. P126974) and the Global Fellowship at the Worcester Polytechnic Institute (WPI), MA, USA.

CONFLICT OF INTEREST

The authors declare no potential conflict of interest.

DATA AVAILABILITY STATEMENT

The data that support the findings of this study are available from the corresponding author upon reasonable request.

REFERENCES

1. Abdulkareem F. Epidemiology & incidence of common cancers in Nigeria. In: Cancer Regist. Epidemiol. Workshop, April 2009, January; 2009:1-58.
2. Azubuike SO, Muirhead C, Hayes L, Mcnally R. Rising global burden of breast cancer: the case of sub-Saharan Africa (with emphasis on Nigeria) and implications for regional development: a review. *World J Surg Oncol*. 2018;16:1-13.
3. Adeloye D, Sowunmi OY, Jacobs W, David RA, Adeosun A, Amuta AO. Estimating the incidence of breast cancer in Africa: a systematic review and meta-analysis. *J Glob Health*. 2018;8(1):010419.
4. Senapati S, Mahanta AK, Kumar S, Maiti P. Controlled drug delivery vehicles for cancer treatment and their performance. *Signal Transduct Target Ther*. 2018;3(1):7.
5. Din FU, Aman W, Ullah I, et al. Effective use of nanocarriers as drug delivery systems for the treatment of selected tumors. *Int J Nanomed*. 2017;12:7291-7309.
6. Yingchoncharoen P, Kalinowski DS, Richardson DR. Lipid-based drug delivery systems in cancer therapy: what is available and what is yet to come. *Pharmacol Rev*. 2016;68(3):701-787.
7. Kydd J, Jadia R, Velpurisiva P, Gad A, Paliwal S, Rai P. Targeting strategies for the combination treatment of cancer using drug delivery systems. *Pharmaceutics*. 2017;9(4):46.
8. Stephen KA. Breast cancer global research: coping, social support and health of women with breast cancer. In: Nursing Research Congress, Cape Town, South Africa, July; 2016:79728.
9. Siegel RL, Miller KD, Jemal A. Cancer statistics, 2015. *CA Cancer J Clin*. 2015;65(1):5-29.
10. Stub T, Quandt SA, Arcury TA, Sandberg JC, Kristoffersen AE. Conventional and complementary cancer treatments: where do conventional and complementary providers seek information about these modalities? *BMC Health Serv Res*. 2018;18:1-9.

15524981, 2022, 12, Downloaded from https://onlinelibrary.wiley.com/doi/10.1002/jbm.b.35124 by Egyptian National Sci. Network (Enstinet), Wiley Online Library on [08/11/2022]. See the Terms and Conditions (https://onlinelibrary.wiley.com/terms-and-conditions) on Wiley Online Library for rules of use; OA articles are governed by the applicable Creative Commons License

11. Tannock IF. Conventional cancer therapy: promise broken or promise delayed? *Lancet*. 1998;351(suppl II):9-16.
12. Damyanov CA, Maslev IK, Pavlov VS. Conventional treatment of cancer realities and problems. *Ann Complement Altern Med*. 2018; 1(1):1-9.
13. Wust P, Hildebrandt B, Sreenivasa G, et al. Review hyperthermia in combined treatment of cancer. *Lancet-Oncol*. 2002;3:487-497.
14. Nurgali K, Jagoe RT, Abalo R. Editorial: adverse effects of cancer chemotherapy: anything new to improve tolerance and reduce sequelae? *Front Pharmacol*. 2018;9:1-3.
15. Hirsch LR, Stafford RJ, Bankson JA, et al. Nanoshell-mediated near-infrared thermal therapy of tumors under magnetic resonance guidance. *PNAS* 2003;100(23):13549-13554.
16. Tohme S, Simmons RL, Tsung A. Surgery for cancer: a trigger for metastases. *Cancer Res*. 2018;77(7):1548-1552.
17. Obayemi JD, Jusu SM, Salifu AA, et al. Degradable porous drug-loaded polymer scaffolds for localized cancer drug delivery and breast cell/tissue growth. *Mater Sci Eng C*. 2020;112:110794.
18. Danyuo Y, Obayemi JD, Dozie-Nwachukwu S, et al. Prodigiosin release from an implantable biomedical device: kinetics of localized cancer drug release. *Mater Sci Eng C*. 2014;42:734-745.
19. Danyuo Y, Dozie-Nwachukwu S, Obayemi JD, et al. Swelling of poly(N-isopropylacrylamide) P(NIPA)-based hydrogels with bacterial-synthesized prodigiosin for localized cancer drug delivery. *Mater Sci Eng C*. 2016;59:19-29.
20. Stewart SA, Dominguez-Robles J, Donnelly RF, Larrañeta E. Implantable polymeric drug delivery devices: classification, manufacture, materials, and clinical applications. *Polymers*. 2018;10(12):1379.
21. Langer R. New methods of drug delivery. *Science (80-)*. 1990; 249(4976):1527-1533.
22. Rajgor N, Patel M, Vh B, College MPP, College NP, Vidhyadham SPS. Implantable drug delivery systems: an overview. *Syst Rev Pharm*. 2011;2:91-95.
23. Kan-dapaah K, Rahbar N, Theriault C, Soboyejo W. Implantable polymer/metal thin film structures for the localized treatment of cancer by joule heating implantable polymer/metal thin film structures for the localized treatment of cancer by joule heating. *J Appl Phys*. 2015;117:1-9.
24. Kumar A, Gupta M. Synthesis and surface engineering of iron oxide nanoparticles for biomedical applications. *Biomaterials*. 2005;26: 3995-4021.
25. Press D. Antitumor effects of inductive hyperthermia using magnetic ferucarbotran nanoparticles on human lung cancer xenografts in nude mice. *Onco Targets Ther*. 2013;6:237-242.
26. Gaitas A, Kim G. Inductive heating kills cells that contribute to plaque: a proof-of-concept. *Peer J*. 2015;28:e929.
27. Zuvin M, Koçak M, Ünal Ö, et al. Nanoparticle based induction heating at low magnitudes of magnetic field strengths for breast cancer therapy. *J Magn Magn Mater*. 2019;483:169-177.
28. Dunklin JR, Forcherio GT, Berry KR, Roper DK. Gold nanoparticle – polydimethylsiloxane thin films enhance thermoplasmonic dissipation by internal reflection. *J Phys Chem C*. 2014;118(14): 7523-7531.
29. Liu X, Shan G, Yu J, et al. Laser heating of metallic nanoparticles for photothermal ablation applications. *AIP Adv*. 2017;7(2):025308.
30. Boca SC, Potara M, Gabudean A, Juhem A, Baldeck PL, Astilean S. Chitosan-coated triangular silver nanoparticles as a novel class of biocompatible, highly effective photothermal transducers for in vitro cancer cell therapy. *Cancer Lett*. 2011;311(2):131-140.
31. He R, Wang YC, Wang X, et al. Facile synthesis of pentacle gold-copper alloy nanocrystals and their plasmonic and catalytic properties. *Nat Commun*. 2014;5:4327.
32. Cabana S, Curcio A, Michel A, Wilhelm C, Abou-Hassan A. Iron oxide mediated photothermal therapy in the second biological window: a comparative study between magnetite/maghemite nanospheres and nanoflowers. *Nanomaterials*. 2020;10(8):1-17.
33. Bertuit E, Benassai E, Mériguet G, et al. Structure-property-function relationships of iron oxide multicore nanoflowers in magnetic hyperthermia and photothermia. *ACS Nano*. 2022;16(1):271-284.
34. Jagtap J, Parchur AK. Photothermal ablation: a perspective on technique. *Intervent Oncol*. 2015;360(3):E141-E147.
35. Qin Z, Bischof JC. Thermophysical and biological responses of gold nanoparticle laser heating. *Chem Soc Rev*. 2012;41:1191-1217.
36. Ariati R, Sales F, Souza A, Lima RA, Ribeiro J. Polydimethylsiloxane composites characterization and its applications: a review. *Polymers*. 2021;13(23):4258.
37. Sales F, Souza A, Araiti R, et al. Composite material of PDMS with interchangeable transmittance: study of optical, mechanical properties and wettability. *J Compos Sci*. 2021;5(4):1-13.
38. Vitro C. Combined effects of X irradiation and hyperthermia (42 and 44 °C) on Chinese hamster cells in vitro. *Radiat Res*. 2014;79(1): 77-88.
39. Song CW, Park H, Griffin RJ, Song CW, Park H, Griffin RJ. Improvement of tumor oxygenation by mild hyperthermia improvement of tumor oxygenation by mild hyperthermia. *Semin Oncol*. 2001;155(4): 515-528.
40. Lerman J, Parness J. *41 – Malignant Hyperthermia*. 6th ed. Elsevier Inc. 2019
41. Beik J, Abed Z, Ghoreishi FS, et al. Nanotechnology in hyperthermia cancer therapy: from fundamental principles to to advanced applications. *J Control Release*. 2016;235:205-221.
42. Gerken M, Afnan R, Dörl J. Adaptive behaviour in chickens in relation to thermoregulation. *Arch Fur Geflugelkd*. 2006;70(5):199-207.
43. Nääs IDA, Romanini CEB, Neves DP, do Nascimento GR, Vercellino RDA. Broiler surface temperature distribution of 42 day old chickens. *Sci Agric*. 2010;67(5):497-502.
44. Charlton M, Stanley SA, Whitman Z, et al. The effect of constitutive pigmentation on the measured emissivity of human skin. *PLoS One*. 2020;15(11):1-9.
45. Vera J, Bayazitoglu Y. Gold nanoshell density variation with laser power for induced hyperthermia. *Int J Heat Mass Transf*. 2009;52(3–4):564-573.
46. Kothandaraman CP. *Fundamentals of Heat and Mass Transfer*. 3rd ed. New Age International; 2006.
47. Reynoso FJ, Lee C, Cheong S-K, Cho SH. Implementation of a multi-source model for gold nanoparticle-mediated plasmonic heating with near-infrared laser by the finite element method. *Med Phys*. 2013; 40(7):73301-73311.
48. Pennes HH. Analysis of tissue and arterid blood temperatures in the resting human forearm. *J Appl Physiol*. 1948;1(2):93-122.
49. Riviere L, Causse N, Lonjon A, Dantras E, Lacabanne C. Specific heat capacity and thermal conductivity of PEEK/Ag nanoparticles composites determined by modulated-temperature differential scanning calorimetry. *Polym Degrad Stab*. 2016;127:98-104.
50. Rossmann C, Haemmerich D. Review of temperature dependence of thermal properties, dielectric properties, and perfusion of biological tissues at hyperthermic and ablation temperatures. *Crit Rev Biomed Eng*. 2014;42(6):467-492.
51. Lang J, Erdmann B, Seebass M. Impact of nonlinear heat transfer on temperature control in regional impact of nonlinear heat transfer on temperature control in regional hyperthermia. *Biomed Eng IEEE Trans*. 1999;46(9):1129-1138.
52. Drizdal T, Togni P, Visek L, Vrba J. Comparison of constant and temperature dependent blood perfusion in temperature prediction for superficial hyperthermia. *Radioengineering*. 2010;19(2):281-289.
53. Sawicki B, Miaskowski A. Nonlinear higher-order transient solver for magnetic fluid hyperthermia. *J Comput Appl Math*. 2014;270:143-151.
54. Duck FA. *Physical Properties of Tissue*. Academic Press; 1990.
55. Zhu Q, Shen Y, Zhang A, Xu LX. Numerical study of the influence of water evaporation on radiofrequency ablation. *Biomed Eng Online*. 2013;12:1-16.
56. Chang IA, Nguyen UD. Thermal modeling of lesion growth with radiofrequency ablation devices. *Biomed Eng Online*. 2004;3:1-19.

15524981, 2022, 12, Downloaded from https://onlinelibrary.wiley.com/doi/10.1002/jbm.b.35124 by Egyptian National Sci. Network (Enstinet), Wiley Online Library on [08/11/2022]. See the Terms and Conditions (https://onlinelibrary.wiley.com/terms-and-conditions) on Wiley Online Library for rules of use; OA articles are governed by the applicable Creative Commons License

57. Chang IA. Considerations for thermal injury analysis for RF ablation devices. *Open Biomed Eng J*. 2010;4:3-12.
58. Van Rhoon GC, Samaras T, Yarmolenko PS, Dewhirst MW, Neufeld E, Kuster N. CEM43°C thermal dose thresholds: a potential guide for magnetic resonance radiofrequency exposure levels? *Eur Radiol*. 2013;23(8):2215-2227.
59. Kan-Dapaah K, Rahbar N, Soboyejo W. Implantable magnetic nanocomposites for the localized treatment of breast cancer. *J Appl Phys*. 2014;116(23):233505.
60. Haemmerich D, Webster J, Mahvi D. Thermal dose versus isotherm as lesion boundary estimator for cardiac and hepatic radio-frequency ablation. In: Eng. Med. Biol. Soc. 2003. Proc. 25th Annu. Int. Conf. IEEE, Vol. 1; 2003:134-137.
61. Murbach M, Neufeld E, Capstick M, et al. Thermal tissue damage model analyzed for different whole-body SAR and scan durations for standard MR body coils. *Magn Reson Med*. 2014;71(1):421-431.
62. Sapareto SA, Dewey WC. Thermal dose determination in cancer therapy. *Int J Radiat Oncol Biol Phys*. 1984;10(6):787-800.
63. Dewhirst M, Viglianti BL, Lora-Michiels M, Hoopes PJ, Hanson MA. Thermal dose requirement for tissue effect: experimental and clinical findings. *Therm Treat Tissue Energy Deliv Assess II*. 2003;4954:37.
64. Groza A, Surmeian A. Characterization of the oxides present in a polydimethylsiloxane layer obtained by polymerisation of its liquid precursor in corona discharge. *J Nanomater*. 2015;2015:1-8.
65. Theriault C, Paetzell E, Chandrasekar R, Barkey C, Oni Y, Soboyejo WO. An in-vitro study of the effects of temperature on breast cancer cells: experiments and models. *Mater Sci Eng C*. 2012;32(8):2242-2249.
66. Wang H-Y, Fu JC-M, Lee Y-C, Lu P-J. Hyperthermia stress activates heat shock protein expression via propyl isomerase 1 regulation with heat shock factor 1. *Mol Cell Biol*. 2013;33(24):4889-4899.
67. Zhao K, Cho S, Procissi D, Larson AC, Kim DH. Non-invasive monitoring of branched au nanoparticle-mediated photothermal ablation. *J Biomed Mater Res – Part B Appl Biomater*. 2017;105(8):2352-2359.
68. Mohammed S, Mohammed H. Characterization of magnetite and hematite using infrared spectroscopy. *Arab J Sci Res Publ*. 2018;2(1):38-44.
69. Kan-Dapaah K, Rahbar N, Tahlil A, Crosson D, Yao N, Soboyejo W. Mechanical and hyperthermic properties of magnetic nanocomposites for biomedical applications. *J Mech Behav Biomed Mater*. 2015;49:118-128.
70. Dutz S, Hergt R. Magnetic nanoparticle heating and heat transfer on a microscale: basic principles, realities and physical limitations of hyperthermia for tumour therapy. *Int J Hyperthermia*. 2013;29(8):790-800.
71. Parkinson P, Lloyd-Hughes J, Gao Q, et al. Transient terahertz conductivity of GaAs nanowires. *Nano Lett*. 2007;7(7):2162-2165.
72. Wang D, Guan J, Hu J, Bourgeois MR, Odom TW. Manipulating light-matter interactions in plasmonic nanoparticle lattices. *Acc Chem Res*. 2019;52(11):2997-3007.
73. Hashimoto S, Werner D, Uwada T. Studies on the interaction of pulsed lasers with plasmonic gold nanoparticles toward light manipulation, heat management, and nanofabrication. *J Photochem Photobiol C Photochem Rev*. 2012;13(1):28-54.
74. Fu S, Man Y, Jia F. Photothermal effect of superparamagnetic Fe_3O_4 nanoparticles irradiated by near-infrared laser. *J Nanomater*. 2020;2020:2832347.
75. Brezovich IA, Atkinson WJ, Lilly MB. Local hyperthermia with interstitial techniques. *Cancer Res*. 1984;44(10 SUPPL):4752-4757.
76. Fekrazad R, Naghdi N, Nokhbatolfoghahaei H, Bagheri H. The combination of laser therapy and metal nanoparticles in cancer treatment originated. *Laser Appl Med Sci Res Cent*. 2016;7(2):62-67.
77. Hudson DE, Hudson DO, Wininger JM, Richardson BD. Penetration of laser light at 808 and 980 nm in bovine tissue samples. *Photomed Laser Surg*. 2013;31(4):163-168.
78. Svobodova B, Kloudova A, Ruzicka J, et al. The effect of 808 nm and 905 nm wavelength light on recovery after spinal cord injury. *Sci Rep*. 2019;9(1):1-14.
79. Konku-Asase YK, Kan-Dapaah K. Plasmonic nanocomposite implants for interstitial thermotherapy: experimental and computational analysis. *Materials*. 2021;14(4):1-16.
80. Mark JE. *Polymer Data*. Oxford University Press; 1999.
81. Greening GJ, Higgins LM, Roblyer D, Pierce MC, Muldoon TJ. Characterization of thin poly simulating phantoms with tunable reduced scattering and absorption coefficients at visible and near-infrared wavelengths. *J Biomed Opt*. 2014;19(11):115002.
82. Weidenfeller B, Höfer M, Schilling F. Thermal and electrical properties of magnetite filled polymers. *Compos Part A Appl Sci Manuf*. 2002;33(8):1041-1053.
83. Daniels C. Electrical field and temperature model of nonthermal irreversible electroporation in heterogeneous tissues. *J Biomech Eng*. 2016;131:1-12.

How to cite this article: Onyekanne CE, Salifu AA, Obayemi JD, et al. Laser-induced heating of polydimethylsiloxane-magnetite nanocomposites for hyperthermic inhibition of triple-negative breast cancer cell proliferation. *J Biomed Mater Res*. 2022;110(12):2727-2743. doi:10.1002/jbm.b.35124

15524981, 2022, 12, Downloaded from https://onlinelibrary.wiley.com/doi/10.1002/jbm.b.35124 by Egyptian National Sci. Network (Enstinet), Wiley Online Library on [08/11/2022]. See the Terms and Conditions (https://onlinelibrary.wiley.com/terms-and-conditions) on Wiley Online Library for rules of use; OA articles are governed by the applicable Creative Commons License